Synchrotron-based investigations of the nature and impact of iron contamination in multicrystalline silicon solar cell materials

Tonio Buonassisi[1,2*], Andrei A. Istratov[1,2], Matthias Heuer[1,3], Matthew A. Marcus[1,6], Ralf Jonczyk[4], Joerg Isenberg[5], Barry Lai[7], Zhonghou Cai[7], Steven Heald[7], Wilhelm Warta[5], Roland Schindler[5], and Eicke R. Weber[2,1]

[1] Lawrence Berkeley National Laboratory, 1 Cyclotron Road, Berkeley, CA 94720

[2] Electronics Research Laboratory, Department of Materials Science and Engineering, University of California, Berkeley, CA 94720

[3] University of Leipzig, Scharnhorststr. 20, D-04275 Leipzig, Germany

[4] GE Energy, 231 Lake Drive, Newark, DE 19702

[5] Fraunhofer Institute for Solar Energy Systems, Heidenhofstrasse 2, D-79110 Freiburg, Germany

[6] Advanced Light Source, Lawrence Berkeley National Laboratory, Berkeley, CA 94720

[7] Advanced Photon Source, Argonne National Laboratory, 401-B3194, 9700 S. Cass Ave., Argonne, IL 60439

PACS: 84.60.Jt; 61.72.-y; 78.70.-g; 82.80.Ej

* Corresponding author: Tonio Buonassisi: Lawrence Berkeley National Laboratory, Mail Stop 62R0203, 1 Cyclotron Road, Berkeley, CA 94720; Phone: +1-510-486-5569; Fax: +1-510-486-4995; Email: buonassisi@alumni.nd.edu

Abstract

Synchrotron-based microprobe techniques were used to obtain precise and systematic information about the size distribution, spatial distribution, shape, electrical activity, and chemical states of iron-rich impurity clusters in multicrystalline silicon materials used for cost-effective solar cells. These experimentally observed properties of iron-rich clusters allow one to derive conclusions about the origins of iron contamination, the mechanisms for incorporating large amounts of Fe into mc-Si, quantitative information about the distribution of Fe in mc-Si and the impacts of such contamination on solar cell performance. Two distinct groups of iron-rich clusters have been identified in both materials: (a) the occasional large (diameter ≥ 1 μm) particles, either oxidized and/or present with multiple other metal species reminiscent of stainless steels or ceramics, which are believed to originate from a foreign source such as the growth surfaces, production equipment, or feedstock, and (b) the more numerous, homogeneously distributed, and smaller iron silicide precipitates (dia. ≤ 800 nm, often < 100 nm), originating from a variety of possible formation mechanisms involving atomically dissolved iron in the melt or in the crystal. It was found that iron silicide nanoprecipitates account for bulk Fe concentrations as high as $10^{14\text{-}15}$ cm^{-3} and can have a large negative impact on device performance because of their homogeneous distribution along structural defects. The large (dia. ≥ 1 μm) particles, while containing elevated amounts of metals, are low in spatial density and thus deemed to have a low direct impact on device performance, although they may have a large indirect impact via the dissolution of Fe, thus assisting the formation of iron silicide nanoprecipitates. These results demonstrate that it is not necessarily the total Fe content that limits mc-Si device performance, but the distribution of Fe within the material.

I. Introduction

In terms of peak power, over 50% of the worldwide solar cell market is based on multicrystalline silicon (mc-Si).[1] It is known that even minute concentrations (< 1 ppb) of iron can drastically reduce the minority carrier diffusion length in p-type silicon, the base material for the vast majority of crystalline silicon photovoltaic (PV) devices. Just ~2×10^{12} cm^{-3} of interstitial Fe (Fe_i) or ~2×10^{13} of iron-boron (Fe_i-B_s) pairs in single-crystalline silicon can reduce the minority carrier diffusion length to 50 μm ($\tau \sim 1$ μs), unacceptable for most PV devices of reasonable efficiencies.[2] Despite this fact, recent neutron activation analysis (NAA) data on commercially-available multicrystalline silicon (mc-Si) solar cell material reveals Fe concentrations of 10^{14} to 10^{16} cm^{-3} (Refs. [3,4]). The question naturally arises as to how mc-Si can contain so much iron yet manage to achieve reasonable operating efficiencies.

The impact of Fe on device performance is shown herein to depend on the nature and the distribution of Fe contamination in mc-Si, rather than the total Fe concentration. Up until recently, a precise experimental determination of the nature and distribution of Fe had been challenging. Although Fe-rich clusters can have a strong impact on electrical measurements, their small size (≤ 100 nm diameter) renders them undetectable to most macroscopic analytical techniques. In addition, their inhomogeneous spatial distribution and relatively low density can make them difficult to detect in transmission electron microscopy. In contrast, synchrotron-based analytical microprobe tools provide both the sensitivity and the large scanning volumes necessary to detect and characterize multiple metal clusters within a silicon matrix, thus deriving statistically meaningful data regarding the recombination activity, size, morphology, and chemical state of nanometer-scale metal impurity clusters with a sub-micron spatial resolution.[5,6] Since the advent of synchrotron-based analytical microprobe techniques, there have been reports of Fe-rich clusters in a variety of mc-Si materials[4-10], yet little effort has been invested into systematically characterizing these clusters and drawing meaningful physical trends from the data.

In this study, synchrotron-based microprobe techniques were applied to draw universal conclusions about the nature of Fe contamination in mc-Si via the systematic characterization of iron-rich precipitates and inclusions affecting two very different types of mc-Si solar cell materials: directionally-solidified cast mc-Si, and AstroPower SiliconFilm™ sheet material. Directionally solidified mc-Si crystal growth, which includes casting[11], is currently well-established and accounts for the vast majority of worldwide mc-Si production.[1] Despite the widespread utilization of this material, regions of low minority carrier diffusion length, characterized by high densities of structural defects such as grain boundaries and dislocations, continue to be a major source of power and efficiency loss.[12,13] SiliconFilm™ sheet material is grown by a different process, involving lower-quality feedstock and high crystal growth rates, which produces 600-800 μm-thick sheets of mc-Si material with grain sizes between 100 μm to 5 mm. [14-16] While such a high throughput, low-cost process has the potential to significantly reduce the price of PV[17], it also results in increased impurity content in the material, including carbon and oxygen related defects[16,18] and transition metals[4,16]. Through the analysis of Fe-rich inclusions and precipitates in both cast and sheet mc-Si materials, certain trends were observed, which elucidate the origins of iron contamination, the mechanisms for incorporating large amounts of Fe into mc-Si, quantitative information about the distribution of Fe in mc-Si and the impacts of such contamination on solar cell performance.

II. MATERIALS AND METHODS:

Cast mc-Si wafers, grown by a commercial supplier, were cut both from vertical and from horizontal slices of the ingot, as depicted in Fig. 1. Some of these wafers were fabricated into solar cells and characterized by Laser-Beam Induced Current (LBIC) at the Fraunhofer Institute for Solar Energy Systems in Freiburg, Germany. Regions of interest towards the bottom of the ingot were selected because of the low LBIC signal indicating poor material performance. Samples approximately 1×1 cm^2 were extracted from these regions of interest in the processed wafers. Similar samples were also extracted from these same locations in the unprocessed sister wafers (i.e. wafers extracted from neighboring slices of the ingot). The metallization and anti-reflection coating of the processed material were removed by etching the samples first in hot mixture 3:1 $HCl:HNO_3$ (at approximately 80°C) and then in a hot phosphoric acid bath (at 160°C). The sheet material used in this study was provided by AstroPower, out of which samples of approximately 1×2 cm^2 were extracted. The samples were then etched slightly in a 1:10 $HF:HNO_3$ mixture to remove any possible surface contamination.

The synchrotrons utilized throughout this study are the Advanced Photon Source (APS) at Argonne National Laboratory, and the Advanced Light Source (ALS) at Lawrence Berkeley National Laboratory. Specifically, ALS Beamlines 10.3.1 (Ref. [19]) and 10.3.2 (Ref. [20]), and APS Beamlines 2-ID-D (Refs. [21,22]) and 20-ID-B (Ref. [23]) were employed in these investigations. At these beamlines, state-of-the-art analytical X-ray microprobes can achieve spot sizes of 200 nm to 5 μm in diameter. A small beam size, high flux, and ultra-low Bremsstrahlung background allow one to achieve the high sensitivity necessary to detect very small metal clusters. On the other hand, given a typical accumulation time at each spot on the order of a second, only small areas of a sample (typically from several hundreds to several thousands of square microns) can be mapped if a step size comparable to the beam size is used. Since the area of a solar cell is much larger, one has to use a complimentary technique to identify the underperforming regions of the cell for further investigation. This can be done by a large, undersampled (i.e., with a step size much larger than the X-ray beam spot size) maps of the minority carrier diffusion length taken in-situ by the X-ray Beam Induced Current technique (XBIC) technique.[9] This technique measures the magnitude of the X-ray stimulated minority carrier flux reaching a Schottky diode or pn-junction. To perform XBIC, aluminum diodes were evaporated onto the front surfaces of the samples over regions of interest. The aluminum diodes, approximately 20 nm thick, were thin enough to ensure the unperturbed transmission of X-rays with energies greater than 1 keV. Due to the similarity of the physical principles of both techniques, XBIC maps can be directly correlated with LBIC maps.[6]

After a region of interest in the sample is identified by XBIC, X-ray fluorescence microscopy (μ-XRF) scans are performed with a much smaller step size to search for metal-rich clusters embedded in the silicon matrix. The detection limit of the μ-XRF technique is dependent upon the spot size, accumulation time, and overall bulk sensitivity of the system, which can depend on the detector, X-ray flux, and geometry of the system.[24] The total number of Fe atoms contained within one precipitate (N_{Prec}) located near the sample surface can be determined via the following equation:

$$N_{\mathrm{Prec}}\,(\mathrm{atoms}) = \frac{C_{\mathrm{Prec}}\,(\mathrm{cts/s})}{C_{\mathrm{Std}}\,(\mathrm{cts/s})} \cdot [\mathrm{Fe}]_{\mathrm{Std}}\,(\mathrm{g/cm^2}) \cdot D_{\mathrm{Std}}\,(\mathrm{atoms/g}) \cdot A\,(\mathrm{cm^2}) \qquad [1]$$

C_{Prec} and C_{Std} correspond to the measured XRF Fe-Kα counts, normalized to acquisition time, for the precipitate of interest and standard sample, respectively. $[\mathrm{Fe}]_{\mathrm{Std}}$ is the areal Fe density in the standard material, which is typically a NIST 1833 foil for X-ray fluorescence calibration, provided by the National Institute of Standards and Technology (NIST). While in the

NIST standard the Fe is in metallic form, theoretically a film of any Fe compound in known concentration could be used, provided it is thin enough such that matrix absorption of Fe-Kα fluorescence does not occur within the film. D_{Std} represents the number of Fe atoms per unit mass of standard material. A is the full width half maximum (FWHM) of the X-ray beam spot size. Additional corrections (not shown here) may be introduced to account for the depth of the precipitate from the sample surface, and for the flare, i.e. the percentage of X-rays falling outside of the FWHM.

To convert N_{Prec} into more meaningful quantities, such as the radius of the precipitate (R_{Prec}, assuming a spherical geometry), the following equation is used:

$$R_{\mathrm{Prec}}\,(\mathrm{cm}) = \left(\frac{3}{4\pi} \cdot \frac{N_{\mathrm{Prec}}\,(\mathrm{atoms})}{D_{\mathrm{Prec}}\,(\mathrm{atoms/cm^3})} \right)^{1/3} \qquad [2]$$

Where D_{Prec} is the density of the compound composing the precipitate, in terms of Fe atoms per unit volume. To accurately determine the volume of a precipitate, it is thus necessary to know its chemical state.

For typical experimental conditions with a 200 nm diameter beam and an accumulation time of 1 second, we have detected iron silicide clusters of radius 23±5 nm, while the noise-limited detection limit for the same conditions was estimated to be 16±3 nm for Fe particles near the sample surface. Because the Fe-Kα fluorescence at 6.4 keV decays exponentially within the silicon matrix with an attenuation length (decay constant) of approximately 36 μm, the sensitivity of μ-XRF decreases for particles embedded deeper within the sample. The depth of the particles from the sample surface can be determined and taken into account during calculations of the particle size by either performing a rotation experiment[25] or by comparing the relative amplitudes of the Fe-Kα and Fe-Kβ peaks in the fluorescence spectra. The latter technique utilizes the fact that Fe-Kα and Fe-Kβ emissions have different energies (6.4 and 7.06 keV, respectively), and thus different attenuation lengths (36 μm and 48 μm, respectively). Particles within one attenuation length from the surface of the sample are easily detected. High-resolution μ-XRF measurements can also elucidate the morphology of these metal-rich clusters, provided they are comparable to or larger than the beam spot size.

After metal-rich clusters of interest are located via μ-XRF, their chemical state is assessed via X-ray absorption microspectroscopy (μ-XAS). By using a monochromator to vary the energy of the X-ray beam with an energy resolution of 1 eV or better, the X-ray absorption spectrum of the iron particle is compared against the absorption spectra of commercially-available standard materials such as Fe_2O_3 and $FeSi_2$. Powder particles from the standard materials are selected to be comparable to or smaller than the beam spot size, in order to avoid overabsorption and hole effects when measuring the μ-XAS spectra in fluorescence and transmission modes, respectively.[26]

By using this suite of x-ray microprobe analytical techniques, the recombination activity, size, morphology, and chemical state of iron-rich nano-clusters in silicon can be studied in-situ with a sub-micron spatial resolution.

III. RESULTS: CAST MC-Si MATERIAL

XBIC maps reveal certain grain boundaries with exceptionally high recombination activity in both processed (Fig. 2a) and unprocessed (Fig. 3a) material. Multiple iron-rich clusters are detected by μ-XRF at these locations, as the maps in Fig. 2b and Fig. 3b demonstrate. These iron-rich clusters populating grain boundaries can be divided into two distinct types, with distinct physical properties. Firstly, while the vast majority of iron-rich clusters are small (e.g. P1, P3,

and P4 in Fig. 2b, and all particles in Fig. 3b), some rare clusters have nearly two orders of magnitude higher μ-XRF Fe counts (e.g. P2 in Fig. 2b; note the log scale of Fe concentration). An analysis by μ-XAS reveals that the clusters with smaller Fe counts are composed of iron-silicide ($FeSi_2$), while the clusters with much larger Fe counts are composed of oxidized iron (Fe_2O_3), as shown in Fig. 4a and 4b, respectively.

The average sizes of these two types of iron-rich cluster also show a clear trend, as revealed by high-resolution μ-XRF line scans. These results, which are tabulated in Table I, indicate that the $FeSi_2$ clusters are indeed smaller than the Fe_2O_3 clusters, as their relative μ-XRF Fe count rate in Fig. 2b would suggest.

The compositions of these clusters also differ, as determined by the μ-XRF point scans. While the Fe_2O_3 clusters show appreciable amounts of other contaminants such as Cr, Mn, and Ca (Fig. 5b), the smaller $FeSi_2$ clusters show none of these above the μ-XRF detection limit (Fig 5a). Only in as-grown material can Ni and Cu be found precipitated in the immediate vicinity of $FeSi_2$ in detectable quantities, but not Cr, Mn, Ti, or Ca.

Additionally, the morphologies and orientations of these two types of cluster are very distinct. The large Fe_2O_3 clusters do not appear to be preferentially oriented along the grain boundary or the crystal growth direction, as evidenced by the nearly symmetric values of their spatial dimensions given in Table I. However, the $FeSi_2$ particles are elongated along the grain boundary only in the direction of crystal growth, by a factor of at least 3-4, as reported in Table I and depicted graphically in Fig. 6. (Note that a spatial dimension in Table I of 200-300 nm corresponds to the diameter of the beam, indicating that these values may in fact be much smaller). The possible nature of these elongated $FeSi_2$ particles is discussed in Section V-B.

The distributions of these clusters also differ. While the large Fe_2O_3 clusters are inhomogeneously distributed, the smaller $FeSi_2$ clusters appear to be more regularly spaced. While high-resolution μ-XRF maps (i.e. Fig. 3, showing (a) XBIC and (b) μ-XRF maps along a recombination-active grain boundary of an as-grown horizontal wafer) typically show some microscopic clustering among $FeSi_2$ nanoprecipitates, on a length scale of 100's of microns, these nanoprecipitates are fairly regularly spaced. Taking into account the attenuation length of the Fe-Kα fluorescence in Si, one calculates a $FeSi_2$ precipitate density of $(1.5\text{-}2)\times10^6$ per cm^2 of grain boundary surface area in Fig. 3, resulting in an average spacing between precipitates of 7-8 μm along the grain boundary.

IV. RESULTS: SHEET MATERIAL

As only the metal clusters that remain after device processing directly affect the performance of the solar cell device, a sample from as-grown sheet material was subject to an aluminum gettering sequence for 4 hrs at 800°C to simulate intense processing. A coarse XBIC scan (Fig. 7) over the front surface (the side opposite to the growth substrate and aluminum layer, i.e. closer to the hypothetical pn-junction, were this material to be fabricated into a solar cell) of the sheet material sample reveals two prominent features of low minority carrier diffusion length that have persisted despite the Al gettering treatment: (a) strongly recombination-active grain boundaries, appearing as dark lines in Fig. 7, and (b) localized intragranular defects, appearing as dark dots within the grains of Fig. 7.

μ-XRF point spectra reveal Fe present en masse at both these locations, with a small contribution from Cr in the case of certain intragranular defects. High-resolution μ-XRF maps reveal that the intragranular defects are irregular in shape and consist of an agglomeration of many nanoparticles, as shown in Figs. 8a and 8b. In the spaces between intragranular defects, where the XBIC signal is higher, no Fe-rich particles are detected. These intragranular defects

may consist of iron precipitated at voids and their associated dislocation bunches, which are known to exist in this material.[16,27] The grain boundaries are also decorated by Fe-rich nanoparticles, as shown in Fig. 8c. The chemical states of these particles were measured by μ-XAS; by comparison with standard material, it is deduced that Fe is most likely to be in the form of iron silicide, as shown in Fig. 8d.

Again, the spacing and average size of the iron silicide precipitates along the grain boundaries of this material were significantly homogeneous. The particle density along the surface of the grain boundary was determined to be within the range of $(1\text{-}2)\times10^7$ cm^{-2}, by counting the number of particles in the μ-XRF image of Fig. 8c and considering the extinction distances of incoming and outgoing X-rays in Si, yielding an average spacing of 2-3 μm between neighboring particles. (Note that this value for the particle density along grain boundaries is consistent with the value of 2×10^7 cm^{-2} obtained by Lu *et al.*[18] on a similar sample via etch pit counting.) The average iron content of each of these precipitates at the grain boundaries was determined, by comparison with standard material and use of Eq. 1, to be $(0.69\text{-}2.1)\times10^6$ Fe atoms. Although cross-sectional samples were not analyzed to determine the real 3-dimensional shape of the $FeSi_2$ grain boundary precipitates, if these are assumed to be spherical, per Eq. 2 they would have radii of approximately 23±5 nm.

Another sheet material sample - which was not subject to an aluminum gettering treatment - was etched severely, removing 25 μm from the front and back surfaces. Large metallic clusters consisting of Fe, Ni, and Cr could be detected on both sides of the sample by μ-XRF. Large areas (1×2 mm^2) of the front and back surfaces were scanned with μ-XRF with a spot size of 5×7 μm^2, so as to determine the spatial density of the intragranular defects. It was found that while the relative composition of these particles remains largely the same (see Fig. 9), their spatial densities are remarkably different. While towards the back surface of the wafer (the side facing the substrate and the last to crystallize) nearly 30 such particles were observed within the 1×2 mm^2 scan area, towards the front surface (the side facing away from the substrate, and the first to crystallize), less than 10 were detected. In addition, the clusters detected on the front side appeared less strongly in μ-XRF mapping, indicating lower impurity concentrations. This can also be observed when comparing μ-XRF point spectra (Fig. 9a). It is also worth noting that this relative concentrations of the three metals shown in Fig. 9a (Cr, Fe, and Ni) are nearly the same as those detected via NAA analyses on this material.[4]

The morphology of these (Cr+Fe+Ni)-rich clusters becomes evident through higher resolution μ-XRF mapping. Shown in Fig. 10 is a high resolution image of one such cluster near the rear surface of the sample. The clusters typically consist of various smaller particles, each measuring some <2-5 μm in diameter, which are agglomerated in loosely-packed clusters measuring up to 50-100 μm across. μ-XAS measurements on at least five of these clusters indicate that Fe is present as $FeSi_2$, as shown in Fig. 9b.

It must also be mentioned that one Fe-rich cluster identified by μ-XRF mapping deviates significantly from the others in terms of morphology, composition, and chemical state. This large Fe-rich particle detected near the rear surface of the as-grown sample measures ~25 μm in diameter (Fig. 11a), and contains no Cr nor Ni above the detection limit. In addition, the μ-XAS spectrum of this particle clearly indicates the presence of Fe_2O_3 (Fig. 11b). The overall density of these particles is believed to be rather low, given the sighting of only one such particle in a scan area larger than 1×1 mm^2.

To summarize, in these sheet material samples four classes of Fe-rich particles have been observed, which can be categorized in accordance with their position within the material and

processing history: Near the front surface of aluminum gettered samples, we observe (1) nanometer-sized iron silicide particles populating the grain boundaries, and (2) micron-sized intragranular defect clusters, each cluster consisting of many Fe-silicide nanoparticles. Towards the back surface of as-grown material, we observe (3) multiple clusters measuring tens of microns across and consisting of micron-sized Fe-Cr-Ni-rich particles, in which the metal species are present as silicides, as well as (4) one sighting of a Fe_2O_3 particle, ~25 μm in diameter, unaccompanied by other metals.

V. DISCUSSION:

Despite the unique growth methods and process histories of the different mc-Si samples analyzed herein, one can observe several systematic similarities and differences in the nature of Fe contamination. For example, the observed Fe-rich clusters can be divided into two distinct groups: (a) larger (dia. ≥ 1 μm), but less common, iron-rich clusters consisting of iron oxide, and/or accompanied by other (often slowly-diffusing) metals reminiscent of stainless steels or ceramics, and (b) smaller (dia. ~ 10's or 100's of nm), but more numerous and distributed, iron silicide particles. Despite these differences, both types of iron-rich cluster were most frequently observed along grain boundaries and other structural defects.

From such trends, one can infer useful information about the origins of metal contamination in mc-Si, the physical mechanisms involved in incorporating large amounts of Fe into mc-Si, and the formation of the iron-rich clusters observed by μ-XRF. Fig. 12 presents a pictorial summary of these processes, which will be explained in detail in the following sections. Subsequently, a discussion of the quantified distribution of iron-rich clusters in the finished material is presented, leading to an assessment of the impacts of Fe contamination on solar cell device performance.

V-A. Origins of metal contamination in mc-Si

Based on experimental evidence herein and on other reports in the literature, one deduces that the origins of metals in most mc-Si materials likely include some combination of the following: Metals dissolved in the silicon feedstock, foreign metallic particles introduced with the feedstock, metals originating from furnace or production equipment, and metals diffusing from the walls of the crucible or growth surfaces. As indicated by the arrows emanating from the right-hand side of Fig. 12 and into the melt and warm crystal, metals can be introduced at various stages of the mc-Si growth process. The following paragraphs explore the experimental evidence that leads to these conclusions.

The hypothesis that foreign particles (originating from the feedstock, production equipment, etc.) are incorporated into the melt is substantiated by the μ-XRF observations of a few metal-rich particles of unusually large sizes (typically ≥ 1 μm, see Figs. 10 and 11a, and Table I). All of these large particles observed have one or both of the following additional characteristics: (a) the coincidence of iron with large amounts of other (often slowly-diffusing) metal species (e.g. Ca, Ti, Cr, Mn, Ni, etc.), the relative proportions of which allude to certain steels or ceramics (e.g. Figs. 5b, 10, 9a) and (b) an oxidized chemical state (e.g. Figs. 4b and 11, and Table I).

This last point is a significant indicator of foreign particles being included in the melt, as it is currently believed that oxidized iron compounds are not thermodynamically favored to form under equilibrium conditions within silicon, since the iron-oxygen binding energy is much weaker than that of silicon-oxygen, and thus iron cannot "out-compete" silicon for the oxygen.[28]

(For additional discussion regarding the formation of oxidized metal compounds in Si, see Ref. [29].) However, an Fe_2O_3 particle inserted into the silicon melt should retain its structural integrity for a limited time, as the melting temperature of Fe_2O_3 is approximately 1565°C, about 150°C above the melting temperature of Si. Nevertheless, because molten Si is a reactive environment, it is extremely likely that these particles will, over time, be etched away by the melt and lead to the formation of smaller, more distributed iron silicide particles.

If a limited amount of iron dissolves from iron oxide particles, then it is likely that an even greater amount of iron should dissolve from large metallic iron and iron silicide particles, given that (a) the melting temperature of iron-silicon alloys is below that of silicon[30], and (b) the binding energy of iron atoms to a metallic iron or an iron silicide particle is weaker than to an iron oxide particle.[5] The large, micron-sized (Fe+Cr+Ni)-rich clusters observed by μ-XRF in sheet material (Fig. 8), the composition of which are very similar to stainless steel (Fig. 9a), were determined by μ-XAS to be composed of $FeSi_2$ (Fig. 9b). One can conclude that this iron was most likely introduced into the melt as metallic stainless steel particles, given that oxide particles are expected to survive the rapid crystallization process. It thus seems very plausible that Fe can dissolve from the micron-sized, unoxidized (Fe+Cr+Ni)-rich clusters during crystal growth and subsequent processing, contaminating nearby structural defects.

The inclusions of large particles show variations in their chemical and elemental compositions, indicating a variety of origins. These particles may originate from the feedstock or furnace parts, as suggested by the observations of stainless steel inclusions. However, those are not the only possible sources of iron. Recent results by Rinio *et al.*[31] suggest that Fe diffuses in from the walls of the casting crucible after the cast mc-Si crystal has solidified but before it has cooled. It must be remembered that iron is present in the silicon nitride crucible lining typically in concentrations as high as parts per million. Impurities likely diffuse not only into the finished crystal, but also into the melt, thereby raising the Fe content of the melt, and likely contributing to $FeSi_2$ nanoprecipitate formation.

It is known from previous work that the complete removal of metals precipitated at structural defects is extremely difficult.[32,33] There are also indications that while material quality can be improved significantly via gettering and hydrogen passivation, the original diffusion lengths of uncontaminated silicon may never be fully recovered.[33,34] Thus, considerable effort should be focused on limiting the number of large iron particles entering the melt, either by identifying and controlling the source of the iron particles (e.g. higher-quality feedstock, crucible lining materials, etc.), separating them from the feedstock (a challenge for non-magnetic austenite), or preventing them from melting. Via these improvements, one can limit the amount of dissolved Fe in the melt, and consequently the concentration of iron silicide nanoprecipitates, as depicted in Fig. 12.

While impeding the introduction of metals into the melt via the feedstock, production equipment, and/or growth surfaces will undoubtedly lead to improved materials, often there are certain limits imposed by economics, materials suppliers, or crystal growth conditions. Other strategies must be developed in parallel to limit the impact of metals on device performance. These require a prerequisite understanding of how large amounts of metals are incorporated into mc-Si, how metal-rich clusters are formed, and how their distribution impacts the electrical properties of the material.

V-B. Incorporation of large amounts of Fe into mc-Si

As shown in Fig. 12, there are (at least) five pathways for incorporating Fe into the warm mc-Si material: (a) direct incorporation of incompletely dissolved foreign metal-rich particles

into the crystal as inclusions, (b) direct precipitation of locally supersaturated iron from the melt, (c) segregation of metals dissolved in the melt to structural defects, (d) incorporation of dissolved Fe in the melt into single-crystalline regions of the material as interstitial atoms, and (e) diffusion of Fe from the growth surfaces into the crystal.

The latter two mechanisms (d and e) are rather limited in their potential to introduce large amounts of Fe into most mc-Si materials. Mechanism (e) only affects the regions of the finished material to which the impurity species can diffuse from the growth surface (typically not more than one cm), thus this mechanism has the potential only to deteriorate the border regions of ingots.[31] For ribbon or sheet materials only fractions of a millimeter thick, however, this may be a motive of concern as the impurity species is more likely to diffuse through the entire thickness of the material. As far as mechanism (d) is concerned, simple equilibrium segregation models alone cannot account for the fact that $10^{14\text{-}16}$ cm^{-3} Fe (Ref. [4]) is present in mc-Si materials. Were the amount of Fe incorporated into the final crystal determined simply by the segregation of iron from the melt into single-crystalline regions (as defined by $k_{Si} = 8\times10^{-6}$, i.e. the ratio of Fe solubilities in the melt and in single crystalline silicon, from Ref. [35]), this would imply that the melt at the solid-liquid interface contained as much as 0.01%-1% Fe! If in fact this much Fe were present, instability in the solid-liquid interface would arise, and certainly columnar crystal growth with centimeter-sized grains would not proceed as desired in the case of cast mc-Si.

The first three mechanisms described in the first paragraph of this section (mechanisms a, b, and c) can in fact account for large amounts (parts per billion/million) of iron being incorporated into mc-Si. Evidence for the inclusion of foreign particles is provided by the μ-XRF and μ-XAS observations of oxidized iron and suspected stainless steel particles in the finished material, as discussed in the previous section. The presence of micron-sized Fe_2O_3 particles at grain boundaries in cast mc-Si (Fig. 2b and Table I) indicates that under certain conditions, foreign particles can become trapped at interruptions in the solid-liquid interface caused by certain structural defects, instead of being pushed forward in the melt by a uniformly advancing solidification front. It is known that slowly-moving solidification fronts tend to push large particles in the melt forward rather than incorporate them into the crystal[36], producing a "snow-plow" effect. Since cast mc-Si growth velocities are on the order of 10 μm/s [Refs. [17,37]], it is unlikely that enormous Fe_2O_3 inclusions (with diameters >> 100 μm) will be found within the lower or middle regions of the crystal; any Fe_2O_3 particles of that size in the melt should first dissolve until they are much smaller in size (e.g. micron-sized), at which point they can be incorporated into the grain boundaries. Further evidence for this "snow-plow" effect, or segregation, of large foreign particles during crystal growth is demonstrated in the sheet material sample, as the (Fe+Cr+Ni)-rich clusters are larger in number and in average size of towards the back surface (the last to solidify) of the material, as shown in Fig. 9a.

As iron-rich particles in contact with the melt dissolve, the dissolved iron content in the melt increases. Furthermore, as crystal growth progresses, the segregation of metals from solid to liquid silicon causes the total metal content in the melt – especially at the solid-liquid interface, depending on convective flows – to increase.[38,39] When high metal contents are present in the melt, the following mechanisms (described in the first paragraph of this section) can result in the incorporation of large amounts of iron into the final crystal: (b) the direct precipitation of locally supersaturated iron from the melt, and (c) the segregation of metals to structural defects.

The direct precipitation of iron from the melt can only occur in special conditions, namely, when the impurity concentration in the melt reaches a critical level, as to promote the onset of a second phase. It is known that when the convective flows in the melt are not sufficient, the impurity concentration at the solid-liquid interface increases as impurities are rejected from

the crystal into the melt. Once the impurity concentration at the interface reaches a critical level, any small perturbation of the interface can result in the precipitation of the metal silicide directly into the crystal.[38,40] While the convective flows within the melt during the casting process are not likely to allow impurities to reach critical levels at the planar interface, this might not be the case near grain boundaries. It is known from the work of Abrosimov *et al*.[41] that a grain boundary reaching the solid-liquid interface causes a localized distortion (dip) occur at the solid-liquid interface. It is conceivable that impurities within this dip may be more sheltered from the convective flow of the melt, wherein they may be able to reach critical concentrations and precipitate directly. The morphology of the precipitates, indicating an abrupt onset and a gradual decay as illustrated in Fig. 6a, may be an indication that locally supersaturated iron at the solidification front precipitates abruptly and tails off.

The last mechanism enabling large amounts of iron to be incorporated into mc-Si is the segregation of metals to structural defects. It is known that the solubility of metals in polysilicon is much higher than in single-crystalline silicon, especially at lower temperatures.[42,43] This can be explained by the interaction of metals with dangling or reconstructed silicon bonds in structural defects (e.g. grain boundaries), as well as the reduction of strain energy from metals settling in a distorted silicon lattice near the structural defects.[42,44] This latter mechanism was originally proposed by Cottrell and Bilby[45] to explain the mechanical hardening of steel by the segregation of carbon atoms to dislocations, and actually observed by Blavette *et al*.[46] via three-dimensional atom probe (3DAP) techniques for the case of boron in Fe-Al intermetallics. It is thus concluded that under certain conditions, metals can form a rather homogeneous coating along certain structural defects, which is typically only a fraction of a monolayer in concentration. Because of the homogeneous distribution along a one- or two-dimensional surface of the structural defect, this concentration of Fe is below the current detection limits of μ-XRF microprobes used in this study, in contrast to easily detected three-dimensional, metal-rich clusters.

The consequence of metal segregation to structural defects is that the *total amount* of metals incorporated into the mc-Si crystal can be much higher than in single-crystalline material. Assuming that iron segregates at grain boundaries at a density of one iron atom per 100-500 silicon atoms (not unreasonable, given experimental observations[43]) and estimating the average density of grain boundaries in a typical sample to be 10 cm^{-1} (i.e. an average of 10 cm of grain boundaries intersecting every 1 cm^2 of sample surface area), one estimates that the total Fe segregated at grain boundaries may reach 10^{14} cm^{-3}. This estimate is comparable with iron concentrations on the order of 10^{14} cm^{-3} measured via NAA for cast mc-Si and EFG materials.[4]

To conclude, large amounts of iron can be incorporated into mc-Si via three primary mechanisms: the direct incorporation of incompletely dissolved large, foreign metal-rich particles into the crystal as inclusions, the possibility of direct precipitation of locally supersaturated iron from the melt at regions of the solid-liquid interface sheltered from the convective flow of the melt, and the segregation of metals to structural defects. All three mechanisms, and especially the latter two, indicate that metals should be present at structural defects already during crystal growth, even before the precipitation of supersaturated dissolved metals.

V-C. Precipitation of dissolved Fe during cooling

As seen in the lower half of Fig. 12, there are multiple direct and indirect pathways leading to the formation of iron silicide nanoprecipitates. The direct pathways include: (a) during crystal growth, via precipitation of locally supersaturated metals from the melt (discussed in the previous section) and (b) during sample cooling, via the precipitation of (supersaturated) dissolved metals in single crystalline regions or at structural defects. All of these mechanisms

require high local iron contents in the melt and/or within the warm crystal, at sufficiently high temperatures for impurity atoms to be mobile.

During sample cooling, supersaturated dissolved metals tend to precipitate at existing defect clusters, or form new ones.[47-49] The actual processes leading to precipitate formation during cooling are complex and not entirely understood, but available data[42] suggest that metals supersaturate faster (i.e. have a stronger temperature dependence of solubility) within regions of the material with fewer structural defects compared to regions with elevated amounts of structural defects. Therefore, a strong driving force exists for supersaturated metals within single crystalline regions to accumulate at grain boundaries and other structural defects during sample cooling. Initially, the distributions of metals at structural defects may be very homogeneous, as described in the discussion on segregation in Section V-B. Eventually however, metals homogeneously distributed in the vicinities of structural defects will also reach critical concentrations, inducing precipitation and leading to the formation of iron silicide clusters. With slow cooling rates and high metal concentrations, a few "large" (10's of nm dia.) metal silicide precipitates are expected to form. On the other hand, faster cools offer less time for supersaturated metals to diffuse and form large clusters, thus favoring a more homogenous distribution of metals along structural defects, either atomically or as smaller precipitates.[50] This dependence of precipitate size on cooling rate is reflected in the two materials analyzed: cast mc-Si is cooled very slowly and forms relatively larger particles with larger spacing in between compared to sheet material, which is grown and cooled comparatively quickly, exhibiting precipitates of closer spacing and smaller average size despite a total Fe content 1-2 orders of magnitude higher than cast.[4]

V-D. Estimation of precipitated iron concentration at intragranular defects and grain boundaries

Despite their small size, iron silicide nanoprecipitates are typically separated by as little as a few microns from their nearest neighbor at structural defects. Due to their high spatial density, it is not unreasonable to propose that they may account for a large percentage of the total iron content in the material. To confirm this hypothesis, a series of calculations were performed using XBIC and standard-calibrated μ-XRF data from Al-gettered sheet material and as-grown cast mc-Si, in order to determine the total concentration and distribution of Fe distributed as iron silicide nanoprecipitates close to the pn junction.

The following equation was used to estimate the average bulk Fe concentration due to intragranular defects (IGDs) in sheet material:

$$[\mathrm{Fe}]_{\mathrm{IGDs}}\ (\mathrm{atoms\ Fe/cm^3}) = \frac{N_{\mathrm{IGD}}\ (\mathrm{atoms\ Fe/IGD}) \cdot \rho_{\mathrm{IGDs}}\ (\mathrm{IGDs/cm^2})}{L_{\mathrm{eff}}\ (\mathrm{cm})} \qquad [3]$$

Where N_{IGD} is the number of Fe atoms per intragranular defect as determined from standard-calibrated μ-XRF maps, ρ_{IGD} is the two-dimensional intragranular defect density as determined from XBIC maps, and L_{eff} is the effective minority carrier diffusion length. XBIC maps contain information on recombination-active defects located within a near-surface layer of a sample with a thickness limited by the attenuation length of the incoming X-rays and by the effective diffusion length of the photogenerated minority charge carriers (L_{eff}). Since typical minority carrier diffusion lengths in mc-Si are much lower than the attenuation length of the X-rays used for these XBIC maps (over 250 μm), the XBIC signal is assumed to be limited only by L_{eff}, and thus the IGD concentration per unit volume is simply $\rho_{\mathrm{IGDs}}/L_{\mathrm{eff}}$.

The value of $[Fe]_{IGDs}$ was calculated to be in the range of (0.1-3)×10^{16} Fe/cm^3, by assuming values of χ_{IGD} in the range of (0.19-1.6)×10^9 atoms Fe/IGD as derived from standard-calibrated μ-XRF maps, ρ_{IGD} of (2.3-3.6)×10^4 IGDs/cm^2 as determined from XBIC maps, and assuming L_{eff} ranging from 15 to 30 μm.

The following equation was used to determine the total bulk Fe concentration distributed in the form of iron silicide nanoprecipitates along grain boundaries (GBs):

$$[\mathrm{Fe}]_{\mathrm{GB}}\ (\text{atoms Fe/cm}^3) = \frac{N_{\mathrm{GB}}\ (\text{atoms Fe/particle}) \cdot \rho_{\mathrm{GB}}\ (\text{particles/cm}^2) \cdot L_{\mathrm{GB}}\ (\text{cm})}{A\ (\text{cm}^2)} \qquad [4]$$

N_{GB} represents the number of Fe atoms per nanoprecipitate along the grain boundary, as determined by standard-calibrated μ-XRF data and Eq. 1 to be (0.69-2.1)×10^6 for sheet material and (2.9-3.6)×10^6 for cast mc-Si. The particle density along the surface of the grain boundary (ρ_{GB}) was determined to be within the range of (1-2)×10^7 cm^{-2} for sheet and (1.5-2)×10^6 cm^{-2} for cast. The total length of grain boundary at the surface of the sample (L_{GB}) within a sample surface area (A) can be determined from XBIC images, such as that in Fig. 3a (an excerpt from a much larger map showing several grain boundaries) or Fig. 7. With these data, $[Fe]_{GB}$ was estimated to be (0.4-2)×10^{15} Fe/cm^3 for sheet material and (0.5-3)×10^{14} Fe/cm^3 for cast.

Previous NAA analyses[4] on these materials indicate total Fe contents of (0.87-1.6)×10^{16} Fe/cm^3 for sheet mc-Si and (4.0-4.7)×10^{14} Fe/cm^3 for cast mc-Si. From Fig. 13, it can be concluded that the total amount of Fe contained in these samples as iron silicide nanoprecipitates is comparable to the total amount of Fe in these samples, as measured by NAA. The iron silicide nanoprecipitates – especially those dispersed homogeneously along the grain boundaries – are extremely difficult to detect with most standard analytical techniques, due to their small spatial dimensions and comparatively large distances separating neighboring particles. Yet, it is precisely this form of Fe – homogeneously distributed in smaller clusters – that has a strong negative impact on the device performance.

V-E. Impact of iron distribution on minority carrier diffusion length

The same number of metal atoms can have a large number of unique spatial distributions. By simply changing the distribution of Fe impurity atoms, one can change the volume of material adversely affected by the impurity atoms, and thus, their impact on device performance.[51] This can be understood by considering a hypothetical silicon sample with 10^{14} cm^{-3} iron-boron pairs (Fe_i-B_s) or interstitial iron (Fe_i). The minority carrier diffusion length in such a sample would be approximately 20 μm or 10 μm, respectively.[2] Now, let us assume these iron atoms are allowed to diffuse towards one another and form precipitates of iron-silicide. If we approximate the new minority carrier diffusion length as the distance between neighboring iron silicide clusters, then it is easy to calculate that if the same amount of iron forms precipitates with diameters of 60 nm, then the diffusion length would be ~30 μm, if precipitates with diameters 350 nm form, the average diffusion length would be ~180 μm, etc. One can quickly see the pattern: with increasing average precipitate size (and decreasing density of precipitates), the minority carrier diffusion length increases. It can thus be concluded that it is the distribution of metals, and not their total bulk concentration, that affects device performance in mc-Si.

The smaller, more distributed iron silicide clusters are believed to have a large impact on solar cell device performance, the reason being the small distance separating adjacent clusters. This is substantiated by the correlation between the recombination active grain boundaries shown in XBIC images of Figs. 1a and 5, and the presence of metal silicide precipitates separated by distances of only a few microns (Figs 2b, 3b and 8c). A model developed by Fedotov *et al*.[52]

predicts that when the distance separating neighboring recombination-active clusters along a grain boundary is less than the minority carrier diffusion length within the grains, the grain boundary becomes noticeably recombination-active for minority carriers. This appears indeed to be the case, as the minority carrier diffusion length within the grains of this region of the sample is determined from LBIC measurements to be >50 μm, while the distance separating neighboring Fe-rich clusters can be as little as a few μm. In addition, recent illuminated lock-in thermography (ILT, Ref. [53]) or light modulated lock-in thermography (LimoLIT, Ref. [54]) measurement techniques developed simultaneously by Fraunhofer ISE and the University of Konstanz, respectively, have indicated that grain boundary recombination is one of the most dangerous power loss mechanisms in mc-Si solar cells operating in 1 Sun conditions.[53-55] To improve solar cell device performance, it is of great interest to understand how to effectively passivate or increase the average distance separating metal-silicide nanopreciptiates as much as possible. Simultaneously, it is desirable that the density of grain boundaries within one minority carrier diffusion length of the pn-junction be as low as possible, a modification only possible in certain materials (e.g. sheet material).

Following similar reasoning, intragranular defects can also have a large negative impact on the minority carrier diffusion length. On average, the minority carrier diffusion length will be limited to half the average distance separating adjacent intragranular defects. This effect can be observed in the XBIC map of Fig. 7, wherein intragranular precipitates (such as those shown in high resolution μ-XRF in Figs. 8a and 8b) appear as localized dark points. Areas containing higher densities of these intragranular defects also exhibit lower XBIC signals. As these intragranular defect clusters appear to consist of iron precipitated at the internal surfaces of voids and their surrounding dislocation networks[16,27], it may be possible to improve material quality by inducing the formation of these voids preferentially towards the back surface of the sample, away from the pn junction.[56]

Much different from the case of iron silicide nanoprecipitates, the micron-sized, isolated iron-oxide and stainless steel inclusions observed in mc-Si material are believed to have a very small *direct* impact on device performance. This is due to the fact that the average distance separating these large metal clusters is often many tens or hundreds of microns, more than the minority carrier diffusion length in those bad regions. Despite the small direct impact on device performance, these micron-sized metal-rich clusters may have a large *indirect* impact on device performance, provided that metals can dissolve from these clusters and create the smaller, more distributed iron-silicide nanoprecipitates.

VI. CONCLUSIONS

While NAA data[3,4] have indicated large metal concentrations in mc-Si, particularly Fe with concentrations as high as $10^{14\text{-}16}$ cm^{-3}, the high minority carrier diffusion lengths observed in these materials are contrary to those expected for single crystalline silicon with comparable metal concentrations.[2] In this present study, correlations between XBIC and μ-XRF maps indicate that the nature and distribution of Fe plays a large role in determining its impact on the minority carrier diffusion length. The metal-rich clusters observed in mc-Si materials were thus classified in a systematic way, elucidating their origins, contamination pathways, formation mechanisms, distributions, and impacts on the solar cell device performance.

The iron-rich clusters analyzed in this study can be divided into two distinct groups: Larger particles (diameter ≥ 1 μm) which are present in rather low spatial densities and are believed to be inclusions originating from foreign sources, e.g. the feedstock, growth surfaces,

and/or production equipment. These inclusions are (a) accompanied by lesser amounts of other metals such as Cr, Ni, Mn, Ti, S, or Ca, suggestive of stainless steels or ceramics, and/or (b) in an oxidized chemical state, both indicators of foreign origins. Smaller (dia. < 800 nm, typically < 100 nm) iron silicide precipitates are also observed, but in much higher spatial densities, separated by as little as a few microns. Despite their small size, a large amount of iron (up to $10^{14\text{-}15}$ cm^{-3}) is estimated to be contained in these iron silicide nanoprecipitates, due to their homogeneous distribution and high spatial density along structural defects.

The chemical and elemental composition of large Fe-rich clusters in mc-Si suggest that iron contamination originates from Fe-rich particles or dissolved iron in the growth surfaces, feedstock, and/or production equipment. Large amounts of Fe can be incorporated into mc-Si primarily via three mechanisms: (a) the inclusion of incompletely dissolved foreign iron-rich particles, (b) the direct precipitation of locally supersaturated iron at the solid-liquid interface in the vicinity of structural defects, and (c) the segregation of iron to structural defects. Once inside the crystal at elevated but decreasing temperatures, dissolved iron can form iron silicide nanoprecipitates via segregation to areas with high densities of structural defects.

Correlations revealing Fe present in regions of lower minority carrier diffusion length indicate that Fe-rich clusters play a direct role in decreasing the performance of mc-Si solar cell devices. However, it is the distribution of Fe-rich clusters, and not necessarily the total Fe content in the samples, that plays a greater role in limiting solar cell device performance. Homogeneously distributed, recombination-active nanoprecipitates separated by only a few microns have a much greater impact on the minority carrier diffusion length than do micron-sized clusters separated by several hundreds of microns. In consequence, it is realized that the iron silicide nanoprecipitates have the greater direct impact on device performance. While the larger, micron-sized Fe-rich clusters and inclusions are deemed to have a small direct impact on device performance because of their low spatial density, they are shown to have a large indirect impact, since dissolved iron from those larger clusters can contribute to the formation of iron silicide nanoprecipitates. Improvements to solar cell device performance are expected if metals can be engineered into distributions that impact device performance less, namely by reducing the spatial density of metal-related defects (precipitates and point defects) within one minority carrier length from the pn junction.

VII. ACKNOWLEDGEMENTS

We thank J. P. Kalejs and T. F. Ciszek for discussions encouraging a holistic view of impurity precipitate formation in perspective of the crystal growth process; Peng Zhang for assistance during a sample preparation session and for fruitful discussions; David Schleuning for probing questions and discussions about statistics; Elizabeth Schäfer for LBIC measurements; W. Schröter for encouraging discussions; M. Rinio, S. Glunz, S. Riepe, C. Ballif, B. Geerligs, D. Macdonald, and S. Peters for many illuminating discussions about solar cells and defects in cast mc-Si; Matthew D. Pickett for review of the manuscript. This work was funded by NREL subcontract AAT-2-31605-03, and the AG-Solar project of the government of Northrhein-Westfalia (NRW), funded through the Fraunhofer Institute for Solar Energy Systems (ISE) (Germany). M. Heuer thanks the Deutsche Forschungsgemeinschaft for funding the project HE 3570/1-1. The operations of the Advanced Light Source at Lawrence Berkeley National Laboratory are supported by the Director, Office of Science, Office of Basic Energy Sciences, Materials Sciences Division, of the US Department of Energy under Contract No. DEAC03-76SF00098. Use of the Advanced Photon Source was supported by the US Department of

Energy, Office of Science, Office of Basic Energy Sciences, under Contract No. W-31-109-ENG-38.

REFERENCES:

[1] "Trends in Photovoltaic Applications - Survey report of selected IEA countries between 1992 and 2002," (2003).

[2] A. A. Istratov, H. Hieslmair, and E. R. Weber, Applied Physics A: Material Science & Processing **70,** 489 (2000).

[3] D. Macdonald, A. Cuevas, A. Kinomura, Y. Nakano, in *29th IEEE Photovoltaic Specialists Conference* (New Orleans, USA, 2002), p. 1707.

[4] A. A. Istratov, T. Buonassisi, R. J. McDonald, A. R. Smith, R. Schindler, J. A. Rand, J. P. Kalejs, E. R. Weber, Journal of Applied Physics **94,** 6552 (2003).

[5] S. A. McHugo, A. C. Thompson, A. Mohammed, G. Lamble, I. Périchaud, S. Martinuzzi, M. Werner, M. Rinio, W. Koch, H.-U. Höfs, and C. Häßler, Journal of Applied Physics **89,** 4282 (2001).

[6] T. Buonassisi, O. F. Vyvenko, A. A. Istratov, E. R. Weber, G. Hahn, D. Sontag, J. P. Rakotoniaina, O. Breitenstein, J. Isenberg, and R. Schindler, Journal of Applied Physics **95,** 1556 (2004).

[7] S. A. McHugo, A. C. Thompson, I. Périchaud, and S. Martinuzzi, Applied Physics Letters **72,** 3482 (1998).

[8] A. A. Istratov, H. Hieslmair, O. F. Vyvenko, E. R. Weber, and R. Schindler, Solar Energy Materials & Solar Cells **72,** 441 (2002).

[9] O. F. Vyvenko, T. Buonassisi, A. A. Istratov, H. Hieslmair, A. C. Thompson, R. Schindler, and E. R. Weber, Journal of Applied Physics **91,** 3614 (2002).

[10] T. Buonassisi, O. F. Vyvenko, A. A. Istratov, E. R. Weber, Z. Cai, B. Lai, T. F. Ciszek, and R. Schindler, Physica B **340-342,** 1137 (2003).

[11] A. Schönecker, L. J. Geerligs, and A. Müller, Solid State Phenomena **95-96,** 149 (2003).

[12] B. Sopori and W. Chen, Journal of Crystal Growth **210,** 375 (2000).

[13] J. Isenberg, J. Dicker, S. Riepe, C. Ballif, S. Peters, H. Lautenschlager, R. Schindler, and W. Warta, in *29th IEEE Photovoltaic Specialists Conference* (Piscataway, NJ, 2002), p. 198.

[14] R. B. Hall, A. M. Barnett, S. R. Collins, J. C. Checchi, D. H. Ford, C. L. Kendall, J. Rand, and C. B. Moore, in *US Patent Office* (AstroPower Inc., USA, 2000).

[15] J. S. Culik, I. S. Goncharovsky, J. A. Rand, and A. M. Barnett, Progress in Photovoltaics **10,** 119 (2002).

[16] J. Rand, G. A. Rozgonyi, R. Jonczyk, S. Batta, J. Lu, R. Reedy, and R. Zhang, in *12th Workshop on Crystalline Silicon Solar Cell Materials and Processes*, edited by B. L. Sopori (Breckenridge, CO, 2002).

[17] T. Ciszek, in *Crystal Growth Technology*, edited by T. Fukuda (John Wiley and Sons, Ltd., Sussex, U.K., 2003), p. 267.

[18] J. Lu, M. Wagener, G. Rozgonyi, J. Rand, and R. Jonczyk, Journal of Applied Physics **94,** 140 (2003).

[19] J. H. Underwood, A. C. Thompson, Y. Wu, R. D. Giauque, K. W. Jones, and M. L. Rivers, Nuclear Instruments and Methods in Physics Research Section A: Accelerators, Spectrometers, Detectors and Associated Equipment **266,** 318 (1988).
[20] M. A. Marcus, A. A. MacDowell, R. Celestre, E. Domning, K. Franck, A. Manceau, G. Morrison, T. Miller, H. A. Padmore, and R. E. Sublett, J. Synchrotron Radiation **11,** 239 (2004).
[21] Z. Cai, B. Lai, W. Yun, I. McNulty, A. Khounsary, J. Maser, P. Ilinski, D. Legnini, E. Trakhtenberg, S. Xu, B. Tieman, G. Wiemerslage, and E. Gluskin, AIP Conference Proceeedings **521,** 31 (2000).
[22] W. Yun, B. Lai, Z. Cai, J. Maser, D. Legini, E. Gluskin, Z. Chen, A. Krasnoperova, Y. Valdimirsky, F. Cerrina, E. D. Fabrizio, and M. Gentili, Review of Scientific Instruments **70,** 2238 (1999).
[23] S. M. Heald, E. A. Stern, D. Brewe, R. A. Gordon, E. D. Crozier, D. Jiang, and J. O. Cross, J. Synchrotron Rad. **8,** 342 (2001).
[24] S. A. McHugo, A. C. Thompson, C. Flink, E. R. Weber, G. Lamble, B. Gunion, A. MacDowell, R. Celestre, H. A. Padmore, and Z. Hussain, Journal of Crystal Growth **210,** 395 (2000).
[25] O. F. Vyvenko, T. Buonassisi, A. A. Istratov, and E. R. Weber, Journal of Physics: Condensed Matter **16,** S141 (2004).
[26] A. Manceau, M. A. Marcus, and N. Tamura, in *Applications of synchrotron radiation in low-temperature geochemistry and environmental science*, edited by N. C. Sturchio (Mineralogical society of America, Washington, D.C., 2002), p. 341.
[27] R. Zhang, G. Duscher, J. Rand, and G. A. Rozgonyi, in *12th Workshop on Crystalline Silicon Solar Cell Materials and Processes*, edited by B. Sopori (Breckenridge, CO, 2002), p. 206.
[28] *CRC Handbook of Chemistry and Physics, 84th Edition* (CRC Press, USA, 2003).
[29] T. Buonassisi, M. Marcus, A. Istratov, M. Heuer, T. Ciszek, B. Lai, C. Zhonghou, and E. R. Weber, to be published (2004).
[30] T. B. Massalski, H. Okamoto, P. R. Subramanian, and L. Kacprzak, *Binary Alloy Phase Diagrams* (ASM International, Materials Park, 1990).
[31] M. Rinio, C. Ballif, and T. Buonassisi, in *Defects in the deteriorated border layer of block-cast multicrystalline silicon ingots*, Paris, France, 2004.
[32] S. A. McHugo, H. Hieslmair, and E. R. Weber, Applied Physics A: Material Science & Processing **64,** 127 (1997).
[33] S. A. McHugo, Applied Physics Letters **71,** 1984 (1997).
[34] M. Kittler and W. Seifert, Solid State Phenomena **95-96,** 197 (2004).
[35] S. Mahajan and K. S. S. Harsha, *Principles of Growth and Processing of Semiconductors* (WCB/McGraw-Hill, USA, 1999).
[36] D. R. Uhlmann, B. Chalmers, and K. A. Jackson, Journal of Applied Physics **35,** 2986 (1964).
[37] J. P. Kalejs, Solid State Phenomena **95-96,** 159 (2004).
[38] P. S. Ravishankar, J. P. Dismukes, and W. R. Wilcox, Journal of Crystal Growth **71,** 579 (1985).
[39] B. Chalmers, Journal of Crystal Growth **82,** 70 (1987).
[40] J. P. Kalejs, B. Bathey, and C. Dubé, Journal of Crystal Growth **109,** 174 (1991).
[41] N. V. Abrosimov, A. V. Bazhenov, and V. A. Tatarchenko, Journal of Crystal Growth **82,** 203 (1987).

[42] R. C. Dorward and J. S. Kirkaldy, J. Mater. Sci. **3,** 502 (1968).
[43] A. A. Istratov, W. Huber, and E. R. Weber, Submitted to Appl. Phys. Lett. (2004).
[44] D. West, S. K. Estreicher, S. Knack, and J. Weber, Phys. Rev. B **68,** 035310 (2003).
[45] A. H. Cottrell and B. A. Bilby, Proceedings of the Physical Society: Section A **62,** 49 (1949).
[46] D. Blavette, E. Cadel, A. Fraczkiewicz, and A. Menand, Science **286,** 2317 (1999).
[47] W. C. Dash, Journal of Applied Physics **27,** 1193 (1956).
[48] E. Nes and G. Lunde, Journal of Applied Physics **43,** 1835 (1972).
[49] W. T. Stacy, D. F. Allison, and T. C. Wu, Journal of the Electrochemical Society **129,** 1128 (1982).
[50] A. A. Istratov, T. Buonassisi, M. A. Marcus, T. F. Ciszek, and E. R. Weber, 14th NREL Workshop on Crystalline Silicon Solar Cell Materials and Processes (2004).
[51] P. S. Plekhanov, R. Gafiteanu, U. M. Gosele, and T. Y. Tan, Journal of Applied Physics **86,** 2453 (1999).
[52] A. Fedotov, B. Evtody, L. Fionova, J. Iliashuk, E. Katz, and L. Poljak, Journal of Crystal Growth **104,** 186 (1990).
[53] J. Isenberg and W. Warta, Journal of Applied Physics **95,** 5200 (2004).
[54] M. Kaes, S. Seren, T. Pernau, and G. Hahn, Progress in Photovoltaics: Research and Applications **12,** 355 (2004).
[55] J. Isenberg and W. Warta, Progress in Photovoltaics: Research and Applications **12,** 339 (2004).
[56] S. A. McHugo, E. R. Weber, S. M. Myers, and G. A. Petersen, Applied Physics Letters **69,** 3060 (1996).

Table I:

Cluster Label	Chemical State	X-diameter (nm)	Z-diameter (nm)
P1	$FeSi_2$	290	547
P2	Fe_2O_3	1250	892
P3	$FeSi_2$	≤200	710
P4	$FeSi_2$	275	772
P5	Fe_2O_3	~1450	~1800
P6	$FeSi_2$	≤200	570

Table I. Dimensions and chemical states of various Fe-rich clusters detected by μ-XRF along a strongly recombination-active grain boundary in cast mc-Si material. Dimensions "X" and "Y" are perpendicular to the crystal growth direction of the directionally-solidified cast multicrystalline silicon ingot, while "Z" is parallel to the growth direction, as shown by Fig. 1 and the insets in Fig. 6. Dimensions were determined by the full-width-half-maximum of the Fe concentration extracted from high-resolution μ-XRF line scans, while chemical states were measured with μ-XAS. Notice the elongation of $FeSi_2$ clusters along the crystal growth direction (Z-dimension). Clusters P1 through P4 are shown in Fig. 2, and line scans across P3 are shown in Fig. 6. Note also that the beam spot size is roughly 200 nm, thus dimensions given as 200-300 nm may in reality be much smaller.

Figures for **"Synchrotron-based investigations of the nature and impact of iron contamination in multicrystalline silicon solar cell materials", Buonassisi, Istratov et al.**

Figure 1

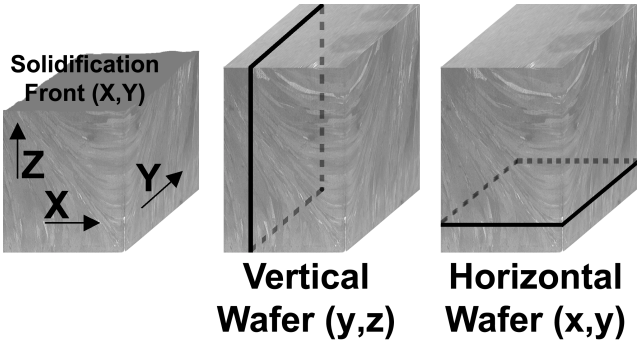

Figure 2

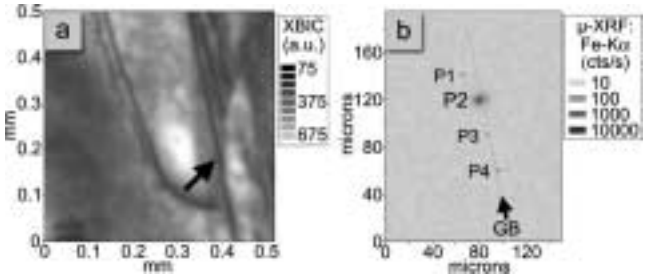

Figure 3

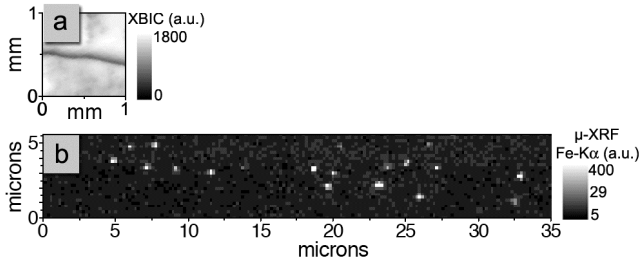

Figure 4

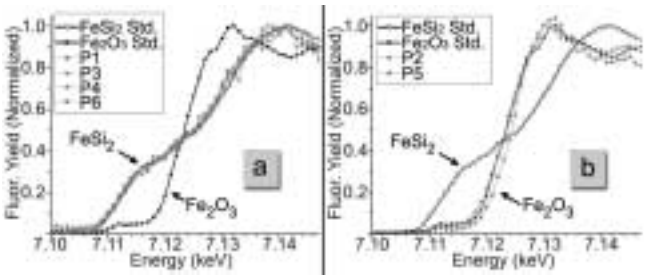

Figure 5

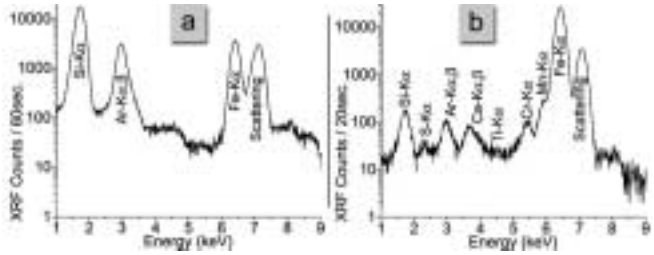

Figure 6

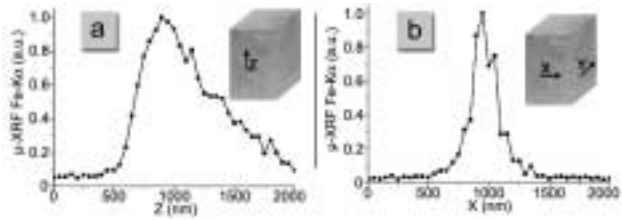

Figure 7

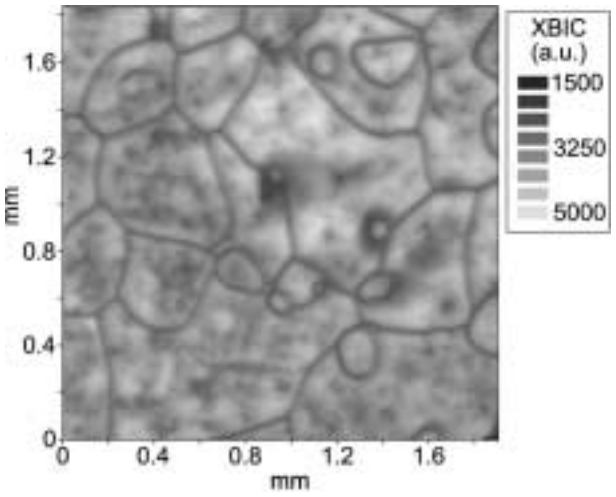

Figure 8

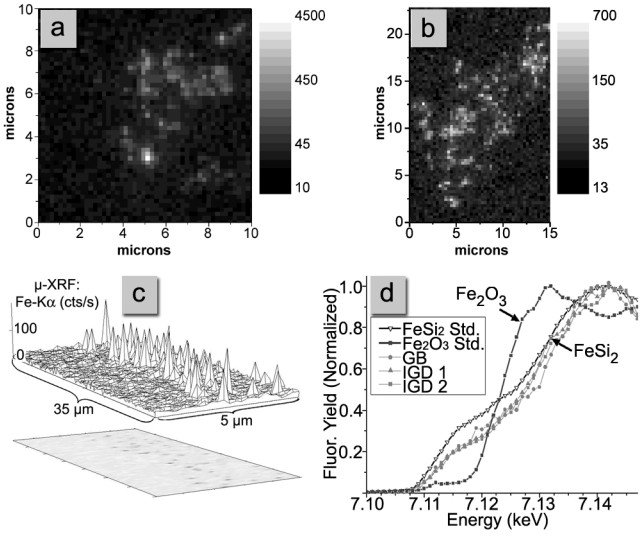

Figure 9

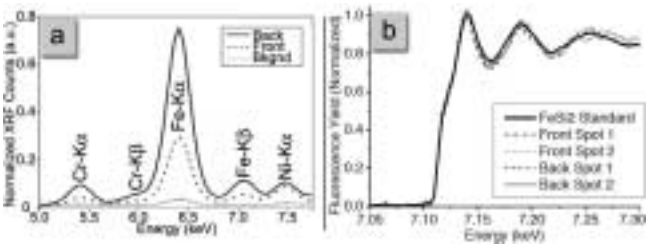

Figure 10

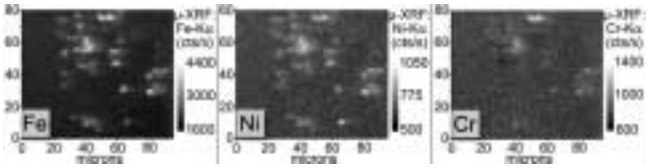

Figure 11

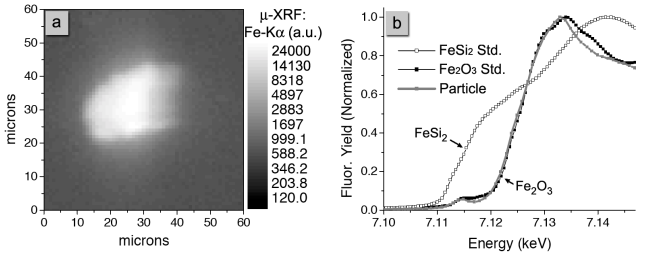

Figure 12

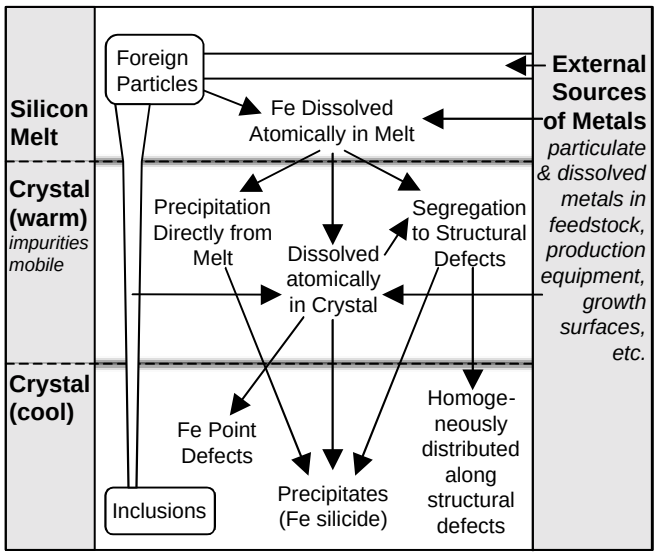

Figure 13

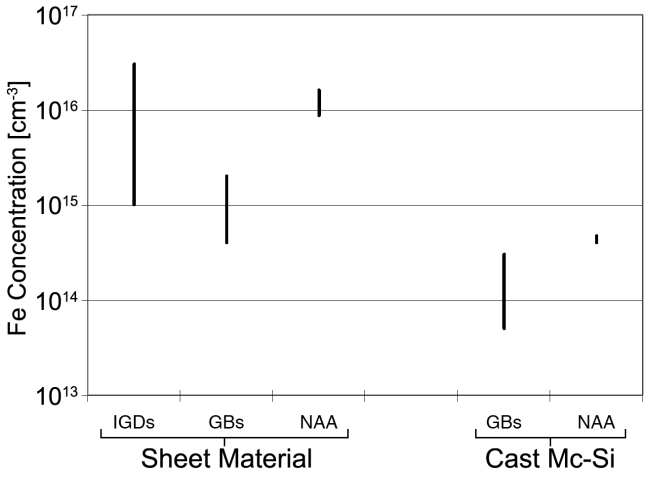

Figure 1: Pictorial representation of the cast multicrystalline silicon ingot. The "Z" coordinate depicts the crystal growth direction, while the "X-Y" plane represents the solidification front. From this ingot, vertical (middle) and horizontal (right) wafers can be extracted.

Figure 2: (a) Typical XBIC image of a cast mc-Si sample extracted from a fully-processed vertical wafer (i.e. parallel to the growth direction of the directionally solidified cast ingot) near the bottom of the ingot. The arrow in (a) points to a recombination-active grain boundary, a region of which was analyzed by μ-XRF in (b). Fe-rich clusters are found along the grain boundary, highlighted by the arrow and the dotted line in (b). Properties of the Fe-rich cluster labeled "P1" through "P4" are summarized in Table I. Note the log scale of μ-XRF Fe-Kα signal intensity, indicating that P2 has approximately two orders of magnitude higher counts than the others.

Figure 3: (a) Large area XBIC and (b) high-resolution μ-XRF map of the iron distribution at a grain boundary in as-grown cast mc-Si. Several $FeSi_2$ nanoprecipitates are observed. Although some clustering is evident on a micron-scale, on a larger scale these $FeSi_2$ nanoprecipitates are distributed rather homogeneously.

Figure 4: μ-XAS data discern two types of Fe-rich cluster in cast mc-Si material: (a) smaller iron silicide ($FeSi_2$) and (b) larger iron oxide (Fe_2O_3). Data labels correspond to precipitates viewed in the μ-XRF image Fig. 1b, and parameterized in Table I.

Figure 5: Typical μ-XRF point scans for the two types of Fe-rich clusters in cast mc-Si: (a) Smaller $FeSi_2$ clusters, without detectable quantities of other metals, and (b) larger Fe_2O_3

particles, wherein iron is accompanied by other elements reminiscent of ceramics, dirt, and stainless steel.

Figure 6: An example of high-resolution μ-XRF line scans across the $FeSi_2$ nanoparticles at a grain boundary in cast mc-Si. In both line scans, the beam size is 200 nm, and step size is 50 nm. The Z dimension corresponds to the crystal growth direction of the cast multicrystalline silicon ingot, while X and Y are perpendicular to the growth direction, as shown in Fig. 1. A curious morphology of these nanoparticles is noted: While the particle appears thin and symmetric in the dimensions of X (shown in (b)) and Y (not shown), indicating that in these dimensions the particle is equal to or smaller than the beam spot size of 200 nm, the Z dimension (along the growth direction) shows a rather abrupt increase followed by a tailing off of the Fe concentration. A possible formation mechanism for these $FeSi_2$ nanoparticles is discussed in the text.

Figure 7: XBIC map of a typical region of Al-gettered sheet material. Features of interest include recombination active grain boundaries and point-like intragranular defects. Dark regions in the map correspond to the areas with high recombination activity.

Figure 8: (a, b) μ-XRF maps of the Fe distribution within typical intragranular defects in sheet material, noted by points of lower XBIC signal in Fig. 5. These defects consist of irregularly-shaped, micron-sized clusters of Fe nanoparticles, and make the largest contribution to the total metal content in this sample. (c) μ-XRF map of Fe nanoparticles within a typical grain boundary, shown in 3D (above) and in 2D projection (below). Although each Fe nanoparticle at the grain boundary is only ~23±5 nm in radius, these nanoparticles are also believed to contain a sizeable

fraction of the total Fe in this sample, due to their high spatial density. (d) The chemical state of the Fe particles shown in (a-c) is revealed by μ-XAS to be most similar to $FeSi_2$.

Figure 9: (a) μ-XRF point spectra of Cr/Fe/Ni-rich particles in the front and back sides of an as-grown sheet material sample. The similar composition of these particles is noted, although the particle on the back surface yields a larger XRF signal, indicating more metals are present. (b) The chemical state of the Fe in such particles found on both the back and front surfaces of the sample is revealed by μ-XAS to be $FeSi_2$. The coincidence of these three metals in the observed proportions suggests contamination by stainless steel; one can conclude from the μ-XAS spectra that these particles were likely introduced in metallic form, and not as oxides.

Figure 10: μ-XRF mapping reveals the Fe, Ni, and Cr distributions at a large defect cluster in as-grown sheet material. The entire defect cluster spans many tens of microns, with a few hundred microns between clusters. Because metals are concentrated in such clusters, the spaces in between the clusters can achieve reasonable minority carrier diffusion lengths. It is thus not the total metal content, but its distribution, that can limit material performance.

Figure 11: (a) μ-XRF and (b) μ-XAS of an oxidized iron particle in as-grown sheet material. Note the large size of this particle (dia. ~ 25 μm), relative to the iron silicide nanoprecipitates (Fig. 8). Such a particle, with large size and oxidized chemical state, is most likely to be an inclusion.

Figure 12: Graphical representation of Sections V-A through V-C, showing the origins of Fe contamination in mc-Si (Section V-A), the physical mechanisms responsible for incorporating

large amounts of Fe into the mc-Si material when warm, i.e. temperatures at which impurity atoms are mobile (Section V-B), and the formation mechanisms of the Fe-rich clusters one observes in finished mc-Si material (Section V-C). Two types of Fe-rich cluster are observed in finished material: inclusions of foreign particles introduced into the melt, and iron silicide nanoprecipitates formed from dissolved iron. Note that the partial or complete dissolution of the former can contribute to the formation of the latter.

Figure 13: Estimated iron contained in $FeSi_2$ nanoprecipitates along grain boundaries (GBs) and at intragranular defects (IGDs) obtained from quantified μ-XRF data for a processed mc-Si sheet material sample (Fig. 6). Also shown is the total Fe content measured by neutron activation analysis (NAA) for a comparable sample, from Ref. [4]. Despite the tiny size of $FeSi_2$ precipitates (typical dia. $\leq$ 50 nm), which renders them undetectable by most standard characterization techniques, their high spatial density results in a large bulk concentration.